Ultrasonics 62 (2015) 299–304

Contents lists available at ScienceDirect

Ultrasonics

journal homepage: www.elsevier.com/locate/ultras

Towards clinical computed ultrasound tomography in echo-mode: Dynamic range artefact reduction

Michael Jaeger *, Martin Frenz

Institute of Applied Physics, University of Bern, Sidlerstrasse 5, 3012 Bern, Switzerland

ARTICLE INFO

Article history:
Received 6 February 2015
Received in revised form 21 May 2015
Accepted 4 June 2015
Available online 10 June 2015

Keywords:
Diagnostic
Multimodal
Reflection mode
Sound speed
Tissue characterisation

ABSTRACT

Computed ultrasound tomography in echo-mode (CUTE) allows imaging the speed of sound inside tissue using hand-held pulse-echo ultrasound. This technique is based on measuring the changing local phase of beamformed echoes when changing the transmit beam steering angle. Phantom results have shown a spatial resolution and contrast that could qualify CUTE as a promising novel diagnostic modality in combination with B-mode ultrasound. Unfortunately, the large intensity range of several tens of dB that is encountered in clinical images poses difficulties to echo phase tracking and results in severe artefacts. In this paper we propose a modification to the original technique by which more robust echo tracking can be achieved, and we demonstrate in phantom experiments that dynamic range artefacts are largely eliminated. Dynamic range artefact reduction also allowed for the first time a clinical implementation of CUTE with sufficient contrast to reproducibly distinguish the different speed of sound in different tissue layers of the abdominal wall and the neck.

1. Introduction

Ultrasound (US) offers flexible probe guidance, real-time display, comparably low cost, and portability for bed-side and emergency use. In order to pair these advantages with outstanding diagnostic power, much effort has been put in complementing classical grey-scale B-mode US with multimodal structural and functional information. This includes Doppler flow imaging, but also novel techniques such as ultrasound elastography [1,2] or optoacoustic imaging [3,4]. A further promising modality is speed of sound imaging. Speed of sound varies significantly depending on tissue type [5,6] and thus its local magnitude can reveal disease-related changes in tissue composition [7,8]. Ultrasound computed tomography (UCT) reconstructs a map of the local speed of sound, based on the arrival time of US pulses that are transmitted through the tissue from various directions. UCT has demonstrated the diagnostic potential of speed of sound imaging as cancer-related changes in tissue composition can be detected with high contrast and spatial resolution [9–13]. On the downside, UCT has several disadvantages compared to conventional US that limit its clinical application: (i) It relies on ultrasound through-transmission and is thus limited to the acoustically transparent breast, whereas other body parts contain bones and air that obstruct ultrasound propagation. (ii) UCT requires dedicated and thus expensive equipment. (iii) The rigid arrangement of US transceivers requires an liquid acoustic coupling medium and thus a bulky setup including a heavy reservoir together with filling pumps resulting in limited portability.

To enable speed of sound contrast for a multimodal diagnosis in combination with conventional handheld US, various researchers have proposed techniques for reflection-mode imaging of speed of sound based on the pulse-echo signal. Nonlinear diffraction tomography (NDT) [14,15] is able to simultaneously reconstruct compressibility and mass density (or equivalently speed of sound and impedance), however it requires the detection of low temporal frequencies in the kHz range to image slow spatial variations of the acoustic properties [14]. The array probes used in conventional US have a limited bandwidth with a cut-off towards low frequencies to enable efficient beam-steering, thus they are not suited for implementation of NDT. In addition the complex algorithms needed for NDT do not yet allow video-rate imaging [14]. A different pulse-echo technique for imaging speed of sound is the beam-tracking method [16]. Based on scanning the tissue with acoustic beams with intersecting axes, one for transmission and one for receiving, the time-of-flight of acoustic power coupled from one into the other beam allows the measurement of speed of sound along the propagation path. This principle can be implemented in handheld probes [17], but the spatial resolution and speed of sound contrast are rather limited [18].

* Corresponding author. Tel.: +41 31 631 89 44.
E-mail addresses: Michael.Jaeger@iap.unibe.ch (M. Jaeger), Martin.Frenz@iap.unibe.ch (M. Frenz).

http://dx.doi.org/10.1016/j.ultras.2015.06.003
0041-624X/

To overcome the limitations of previous approaches, we have recently developed computed ultrasound tomography in echo-mode (CUTE) [19]. This technique is based on analysing the changing position of reconstructed (beam-formed) echoes when changing the transmit (Tx) steering angle φ of US transmission into the tissue. Deviations $\Delta c(x,z)$ of the true speed of sound c from the assumed reference value c_0 result in a non-anticipated error $\tau(x,z,\varphi)$ of the time-of-arrival of the Tx wavefront at points (x,z) in the imaging plane (x and z are the lateral and axial coordinates). The difference $\Delta\tau(x,z,\varphi_0,\varphi)$ of this error relative to a reference angle φ_0 is translated to a corresponding shift $\Delta z(x,z,\varphi_0,\varphi)$ of the reconstructed depth of echoes. Detection of this shift allows a tomographic reconstruction of the relative speed of sound $\Delta c(x,z)$ via solving the corresponding inverse problem [19]. Robust determination of the echo shift Δz is possible via the changing local phase of the reconstructed pulse-echo data (echo shift tracking). Similar to UCT, CUTE is thus based on phase-sensitive detection of the changing arrival time of US transmissions from various angles and a subsequent tomographic reconstruction, but local echoes take the role of virtual internal receivers as opposed to the external receivers in UCT. The abundant availability of such echoes provides internal information that allows a tomographic reconstruction from the limited angle range of pule-echo US. Compared to NDT, CUTE is based on the echo shift rather than the echo pulse shape and thus does not require detection of low frequencies. For those reasons CUTE can be implemented as an addition to conventional pulse-echo US in a single device, which solves the disadvantages of UCT and NDT. In the proof-of-principle phantom study we proposed a direct and thus real-time capable inverse problem solution in the Fourier domain and demonstrated a contrast (0.6% of the background speed of sound) and a spatial resolution (1 mm by 3 mm) that are well suited for clinical diagnosis [19].

The good outcome of the proof-of-principle study relied on phantoms that were characterised by a uniform echogenicity. Clinical pulse-echo images, however, show a large dynamic range of echo intensities of several tens of dB's. As a result, the intensity level of strong local echoes is significantly above the background level, such that the sidelobes of the point-spread function (PSF) over-radiate neighbouring echoes. Changing φ while maintaining a constant receive (Rx) aperture leads to a corresponding rotation of the PSF with sidelobes and thus to an apparent motion up and down of the echo phase to the right and left of the centre of strong echoes (see sketch in Fig. 1). This apparent motion significantly disturbs the detection of the echo depth shift and generates errors that have the shape of "butterfly" patterns that result in strong artefacts in the CUTE image.

Fig. 2 illustrates the problems associated with the dynamic range artefacts. Fig. 2a is the B-mode image taken from a gelatine phantom that contained a cylindrical inclusion (12 mm diameter) with a 2% lower speed of sound than the background. Cellulose powder provided diffuse echogenicity, and parallelly aligned sewing threads served as strong reflectors. For pulse-echo data acquisition we used the same system that was described in the proof-of-principle study [19]. It comprises of a Verasonics® V1-64 research US system (Verasonics Inc., WA, USA) in connection with a HDI L7-4 linear vascular probe (ATL Philips, WA, USA). The probe features 128 elements at a 0.29 mm pitch and a 5 MHz centre frequency. The imaging plane of the linear probe was oriented perpendicular to the direction of the cylindrical inclusion and the threads, which are thus visible as a circular area and strong distinct point-like echoes, respectively. Fig. 2b displays a map of the

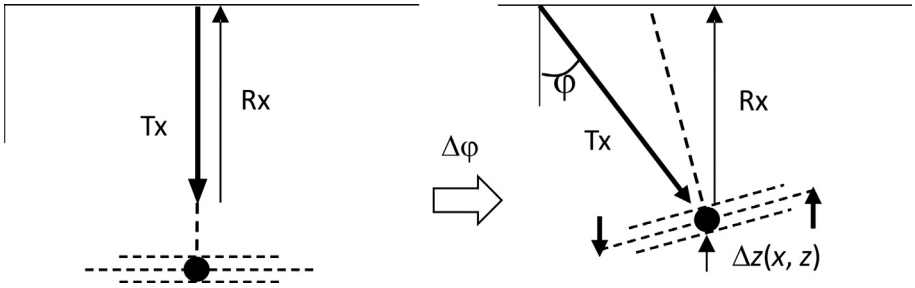

Fig. 1. Sketch of the rotation of the point-spread function (PSF) with the changing transmit steering angle φ. The rotation leads to a motion up and down of the sidelobes of the PSF to the left and right of the centre of the echo. The resulting apparent local echo shift is the sum of the shift of the centre of the echo and the local side-lobe motion.

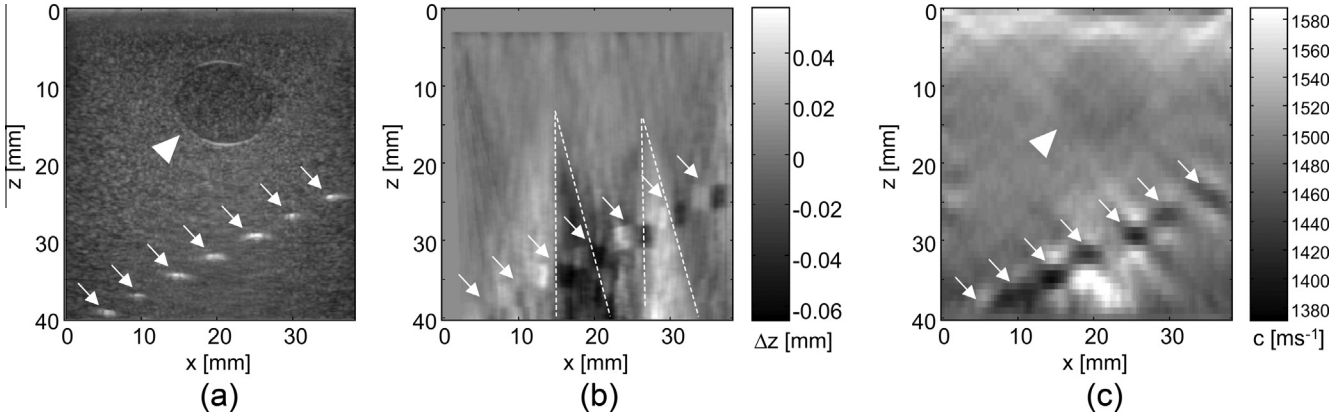

Fig. 2. (a) B-mode US (60 dB range) of a gelatine phantom that contained strong point-like echoes (arrows) as well as a cylindrical inclusion (arrowhead) having a lower speed of sound than the background. (b) The echo shift map when changing the Tx steering angle by 15° reveals the expected shift of local echoes in the shadow of the inclusion (dashed lines). Butterfly-shaped tracking errors are also seen (arrows) that result from the sidelobe rotation at the locations of the strong echoes. (c) As a result of sidelobe rotation, the speed of sound image contains strong cross-shaped artefacts (arrows). The inclusion (arrowhead) is hardly visible.

2-dimensional distribution of the local echo shift $\Delta z(x,z,\varphi_0,\varphi)$ when changing the Tx angle from $\varphi_0 = 0°$ to $\varphi = 15°$. The echo shift map reveals the expected time-of-arrival changes in the "shadow" of the speed of sound contrast of the cylindrical inclusion. In addition, the echo shift map contains the butterfly-shaped tracking errors at the locations of the strong point-like echoes. Using the algorithm described in [19], the relative speed of sound $\Delta c(x,z)$ was reconstructed from a collection of echo shift maps $\Delta z(x,z,\varphi_0,\varphi)$ that were acquired with φ ranging from $-30°$ to $30°$ in $10°$ steps. When added to the reference speed of sound c_0 and displayed in e.g. grayscale, this results in a speed of sound image (Fig. 2c), where the 2-dimensional distribution of the grey level is expected to reveal the speed of sound contrast of the cylindrical inclusion. However, as a result of the butterfly-shaped tracking errors, the contrast is dominated by strong cross-shaped patterns that nearly fully obscure the circular cross-section of the inclusion.

In this paper we propose and investigate a modification to the echo shift tracking, by which butterfly artefacts can be largely eliminated. We demonstrate strongly improved contrast in phantom experiments as well as first promising volunteer results.

2. Method

The proposed modification is based on modelling the effect of sidelobe motion as an additive shift: A hypothetical stand-alone echo located in point (x,z) in the imaging plane leads to a total apparent echo shift $\Delta z'(x',z',\varphi_0,\varphi)$ in points (x',z') inside the surrounding region where no other echo occurs:

$$\Delta z'(x',z',\varphi_0,\varphi) = \Delta z(x,z,\varphi_0,\varphi) + \Delta b(x',z',\varphi_0,\varphi) \tag{1}$$

Thereby Δz is the real shift of the echo owing to the inhomogeneous speed of sound, and Δb is the additive shift owing to rotation of the PSF. Because Δb results from a rotation, its magnitude is proportional to the angle change. It can thus be expressed via a rate b_φ:

$$\Delta z'(x',z',\varphi_0,\varphi) = \Delta z(x,z,\varphi_0,\varphi) + b_\varphi(x',z')\cdot(\varphi-\varphi_0) \tag{2}$$

Eq. (2) describes the apparent local echo shift around a single echo. A typical image contains a large number N of interfering echoes with varying intensity level, centred at different positions $(x,z)_n$ where n is the echo index. In order to employ the model in Eq. (2), we assume that in any point (x',z') the local echo shift is dominated by just one out of these echoes rather than by the superposition of many echoes. We will discuss in Section 4 to what extent this assumption is valid ("condition 1"). The imaging plane is thus organised in grainy image regions that result from the assignment of pixels to different echoes n. We further assume that the boundaries of these image regions do not change with changing φ, such that the rate constant b_φ in any pixel is independent of φ. This is again a strong assumption and will be discussed in Section 4 ("condition 2"). If the echo shift Δz varies on a slower spatial scale than the diameter of the image regions ("condition 3", see Section 4), $\Delta z(x',z',\varphi_0,\varphi)$ can be substituted for $\Delta z(x,z,\varphi_0,\varphi)$ in Eq. (2), and the apparent local shift $\Delta z'$ is described by:

$$\Delta z'(x',z',\varphi_0,\varphi) = \Delta z(x',z',\varphi_0,\varphi) + b_\varphi(x',z')\cdot(\varphi-\varphi_0) \tag{3}$$

Eq. (3) is the foundation of a simple recipe for elimination of the rate constant b_φ: In the following the notation of the spatial coordinates will be omitted. The apparent shift when changing φ from its minimum ($\varphi_{\min}$) to its maximum ($\varphi_{\max}$) value is:

$$\Delta z'(\varphi_{\min},\varphi_{\max}) = \Delta z(\varphi_{\min},\varphi_{\max}) + b_\varphi\cdot(\varphi_{\max}-\varphi_{\min}) \tag{4}$$

Combination of Eqs. (3) and (4) allows the definition of a modified shift $\Delta z''$ in which b_φ is eliminated:

$$\begin{aligned}\Delta z''(\varphi_0,\varphi) &\equiv \Delta z'(\varphi_0,\varphi) - \frac{(\varphi-\varphi_0)}{(\varphi_{\max}-\varphi_{\min})}\Delta z'(\varphi_{\min},\varphi_{\max})\\ &= \Delta z(\varphi_0,\varphi) + b_\varphi\cdot(\varphi-\varphi_0)\\ &\quad - \frac{(\varphi-\varphi_0)}{(\varphi_{\max}-\varphi_{\min})}\left[\Delta z(\varphi_{\min},\varphi_{\max}) + b_\varphi\cdot(\varphi_{\max}-\varphi_{\min})\right]\dots\\ &= \Delta z(\varphi_0,\varphi) - \frac{(\varphi-\varphi_0)}{(\varphi_{\max}-\varphi_{\min})}\Delta z(\varphi_{\min},\varphi_{\max})\end{aligned} \tag{5}$$

For the present study, beam-formed in-phase quadrature (IQ) pulse-echo frames were acquired using Tx angles φ ranging from $-30°$ to $30°$ in $2.5°$ steps. Echo shift tracking was based on tracking the local echo phase by using base-band correlation [20]: The point-wise Hermitian product of successive IQ frames was calculated and spatially low-pass filtered with a box-car convolution kernel with size of 1 mm (laterally) by 3 mm (axially) (tracking kernel). The resulting local correlation phase was then converted to echo shift via multiplication with the spatial oscillation period $\lambda = 0.5\, c_0/f_0$ of local echoes, (f_0: centre frequency). Incremental accumulation of the echo shift per angle step over the full angle range led to maps of the apparent echo shift $\Delta z'(\varphi_0,\ \varphi)$ for all angles φ relative to the reference angle $\varphi_0 = 0°$. Maps of the modified echo shift $\Delta z''(\varphi_0,\ \varphi)$ were then obtained according to the first line in Eq. (5) and used for speed of sound reconstruction.

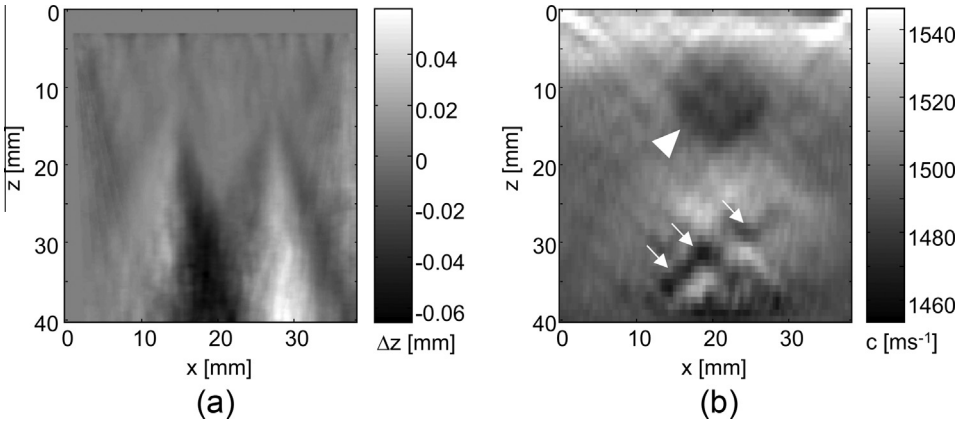

Fig. 3. (a) Modified echo shift map corresponding to (b), but with butterfly tracking errors eliminated. (b) Speed of sound image based on the modified echo shift maps. Artefacts are reduced (arrows) and the inclusion (arrowhead) appears with strongly improved contrast.

3. Results

Fig. 3a is again the echo shift map that was already shown in Fig. 2b, but after modification according to Eq. (5). In this modified data the butterfly-shaped tracking errors are nearly fully eliminated, and the data looks generally less noisy than in Fig. 2b. As a result, the echo shift that was caused by the cylindrical inclusion is clearly visible, and the speed of sound image in Fig. 3b reveals the speed of sound difference inside the inclusion with good contrast. The phantom bulk was made of a homogeneous gelatine solution, thus a constant speed of sound was expected in the background surrounding the inclusion. Even though the background speed of sound appears much more homogeneous in Fig. 3b than in Fig. 2c, some residual artefacts are visible below the inclusion. Potential reasons for these artefacts will be discussed in Section 4.

Similar artefacts to the ones described in the initial phantom speed of sound image (Fig. 2c) were found when imaging the abdominal wall and the neck of a volunteer. Fig. 4a shows the B-mode US of the abdomen, with the skin, subcutaneous adipose, muscle and liver tissue, and Fig. 4b is the B-mode US of the neck, with the nicely delineated sternocleidomastoid muscle as well as less defined deeper muscles. The corresponding speed of sound images (Fig. 4c and d) contain a high level of diagonally running artefacts that limit the contrast of the different tissue layers.

After dynamic range artefact reduction, the contrast of the speed of sound images is strongly improved. Fig. 4e nicely delineates the different speed of sound values in the different layers of the abdominal wall. The speed of sound contrast values indicated by the colour bars is rather qualitative owing to yet unsolved experimental uncertainties (e.g. calibration of the local centre

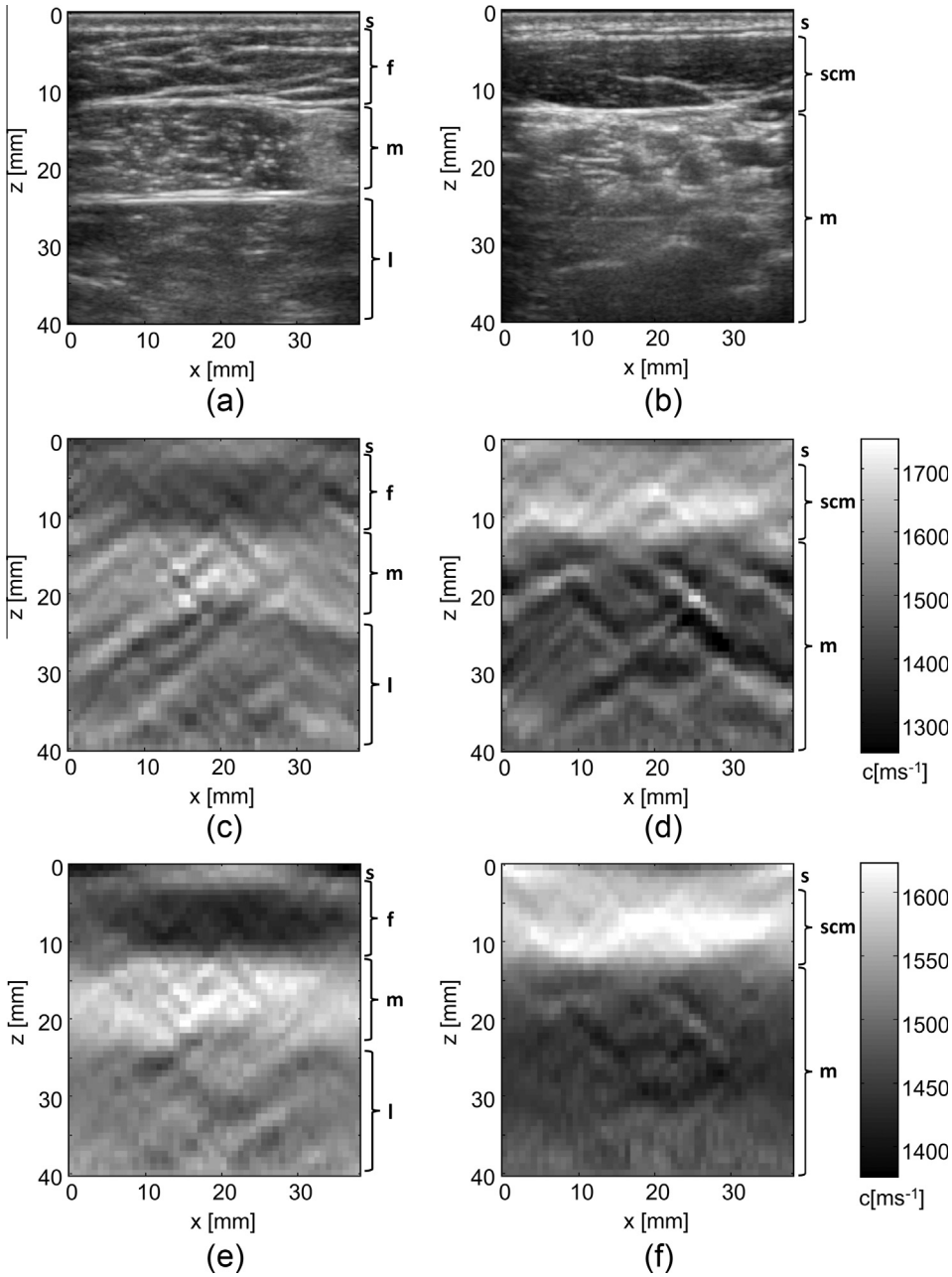

Fig. 4. (a) B-mode US (60 dB) of abdominal wall, showing the skin (*s*), subcutaneous adipose tissue (*f*), musculature (*m*), and liver (*l*), (b) B-mode US (60 dB) of neck, showing the skin (*s*), sternocleidomastoid (scm) and deeper muscles (*m*). (c) and (d) are the speed of sound images without and (e) and (f) with artefact reduction.

frequency...), and appear slightly too large. However, in agreement with the expectations, the skin and the musculature have a relative high, the adipose tissue a low, and the liver tissue an intermediate speed of sound. Fig. 4f interestingly shows a strong speed of sound contrast between the sternocleidomastoid and the deeper muscle layers. This can potentially be attributed to the different composition of fast-twitching (less lipids, higher speed of sound) and slow-twitching (more lipids, lower speed of sound) muscle fibres. According to literature, the speed of sound in muscle tissue can vary by as much as 30 m/s when the lipid concentration differs by 1% of muscle weight [21].

4. Discussion and conclusion

Our results demonstrate that dynamic range artefact reduction is a key step towards successful clinical CUTE. The specific technique that was proposed in this paper was based on several conditions that will be discussed now:

Condition (1): The local echo level in each pixel, and thus the rate b_φ resulting from the echo rotation, was assumed to be dominated by one echo at a time. In any pixel where neighbouring echoes superpose with similar intensity, this assumption will not hold. This is even more the case with the echo shift tracking that measures an average shift of all echoes inside regions of the size of the tracking kernel, rather than the phase shift inside single pixels. However, the phase tracking will just pick out an average echo shift rate, and as long as the relative weights of contributing echoes remain constant, the apparent average rate constant b_φ will not change significantly with changing φ. This leads to:

Condition (2): The respective echo that dominates a pixel (x,z) was assumed independent of φ. Looking at the single pixel level, this assumption seems wrong because with the rotation of the sidelobes, the relative contribution of different echoes will change. However, when averaging over regions of the size of the tracking kernel, the actual condition for the applicability of the model is following: For any pixel (x,z), the average shift in a region (of the size of the tracking kernel) around that pixel is determined by the same relative contribution of the same collection of echoes independent of φ. This condition was roughly fulfilled: A change of the relative contribution of echoes can result from motion of sidelobes into and out of the kernel region. With the 60° Tx angle scanning range, the total rotation of the PSF was 30°. In the phantom study, the total motion of sidelobes of the strongest echoes (around 2 mm lateral extent or 1 mm radius) was therefore only 0.5 mm. In the volunteer study, the lateral extent of strong echoes was even smaller. The total motion of dominating sidelobes was therefore significantly smaller than the axial size of the tracking kernel (3 mm).

Condition (3): The echo shift Δz was assumed to vary on a spatial scale that is slow in comparison to the size of the areas where respective echoes dominate. This was rather a didactic trick that allowed in Eq. (2) the elimination of the ambiguity of the origin (x,z) of an echo and the position (x',z') where the apparent echo shift was evaluated. This assumption was, however, not fundamental to the development of the artefact reduction technique, and the final relation in Eq. (5) without this assumption reads (we leave the derivation to the reader):

$$\Delta z''(x',z',\varphi_0,\varphi) = \Delta z(x,z,\varphi_0,\varphi) - \frac{(\varphi-\varphi_0)}{(\varphi_{\max}-\varphi_{\min})}\Delta z(x,z,\varphi_{\min},\varphi_{\max}) \quad (6)$$

Eq. (6) states that the modified echo shift in a pixel (x',z') is determined by the real echo shift at the origin (x,z) of the respective dominating echo. The modified echo shift is thus constant inside the regions where strong echoes dominate. If the echo shift of the background varies on a faster spatial scale than the lateral extent of these regions, the edges of the regions contrast with the background and lead to a patchy appearance of the echo shift map. This effect is not a result of the artefact reduction technique, but an intrinsic limitation of determining the local echo shift that was already present in Eq. (1).

In summary our results demonstrate that the proposed artefact reduction technique is intriguingly robust even though it was based on a simple model. Residual artefacts can be attributed to sources of tracking errors that were not yet considered, such as acoustic refraction and reverberation clutter. In the phantom result in Fig. 2a, refraction lead to defocusing and thus to broadening of the bright echoes below the cylindrical inclusion. This resulted in a larger sidelobe motion and thus in stronger artefacts below the inclusion than towards the edges of the speed of sound image in Fig. 2c, and might in part explain the residual artefacts below the inclusion in the corrected speed of sound image in Fig. 3b. In addition, refraction can lead to multiple arrivals of the Tx wavefront at echo generating structures and thus to tracking ambiguities that again result in artefacts. Reverberation clutter (higher order echoes) adds to image noise and thus to tracking errors. Whereas clutter was minimised in the phantom study by using a rather low and homogeneous scatter concentration, it is supposed to have been a main source of artefacts in the volunteer images. Further research is therefore required into potential sources of residual artefacts to further improve contrast of CUTE towards a successful diagnostic application. The present study demonstrates that the proposed technique significantly improves the contrast of the speed of sound image and that dynamic range artefact reduction is one key step towards successful clinical CUTE.

Acknowledgements

This study was funded by the Swiss National Science Foundation, through the career development scheme “Ambizione” project PZ00P3_142585 and the NF project 205320-144443. In addition, the research leading to these results has received funding from the European Community's Seventh Framework Program (FP7/2007-2013) under Grant Agreement 318067.

References

[1] A. Thomas et al., Real-time elastography – an advanced method of ultrasound: first results in 108 patients with breast lesions, Ultrasound Obstet. Gynecol. 28 (2006) 335–340.
[2] É. Bavu et al., Noninvasive in vivo liver fibrosis evaluation using supersonic shear imaging: a clinical sudy on 113 hepatitis C virus patients, Ultrasound Med. Biol. 37 (9) (2011) 1361–1373.
[3] M. Heijblom et al., Visualizing breast cancer using the twente photoacoustic mammoscope: what do we learn from twelve new patient measurements?, Opt Express 20 (11) (2012) 11582–11597.
[4] J. Zalev et al., Opto-acoustic breast imaging with co-registered ultrasound, Proc. SPIE 9038 (2014) 90381J.
[5] M.O. Culjat et al., A review of tissue substitutes for ultrasound imaging, Ultrasound Med. Biol. 36 (6) (2010) 861–873.
[6] P.N.T. Wells, Ultrasonic imaging of the human body, Rep. Prog. Phys. 62 (1999) 671–722.
[7] J.C. Bamber, C.R. Hill, Acoustic properties of normal and cancerous human liver-I. Dependence on pathological condition, Ultrasound Med. Biol. 7 (1981) 121–133.
[8] J.C. Bamber, C.R. Hill, J.A. King, Acoustic properties of normal and cancerous human liver-II. Dependence on tissue structure, Ultrasound Med. Biol. 7 (1981) 135–144.
[9] N. Duric et al., Detection of breast cancer with ultrasound tomography: first results with the computed ultrasound risk evaluation (CURE) prototype, Med. Phys. 34 (2) (2007) 773–785.
[10] M. Hollenhorst et al., Ultrasound computed tomography in breast imaging: first clinical results of a custom-made scanner, Ultraschall Med. 31 (2010) 604–609.
[11] G. Zografos et al., Novel technology of multimodal ultrasound tomography detects breast lesions, Eur. Radiol. 23 (2013) 673–683.
[12] J. Wiskin, et al., Three-dimensional nonlinear inverse scattering: quantitative transmission algorithms, refraction corrected reflection, scanner design and

clinical results, in: Proceedings of Meetings on Acoustics, vol 19, 2013, pp. 075001-1–9.
[13] F.M. Hooi, P.L. Carson, First-arrival traveltime sound speed inversion with a priori information, Med. Phys. 41 (8) (2014). p. 082902-1–14.
[14] M.C. Hesse, L. Salehi, G. Schmitz, Nonlinear simultanous reconstruction of inhomogeneous compressibility and mass density distributions in unidirectional pulse-echo ultrasound imaging, Phys. Med. Biol. 58 (2013) 6163–6178.
[15] M.F. Schiffner, G. Schmitz, On the separate recovery of spatial fluctuations in compressibility and mass density in pulse-echo ultrasound imaging using linear inverse scattering, J. Acoust. Soc. Am. 135 (4) (2014). p. 2179–2179.
[16] J. Ophir, Estimation of the speed of ultrasound propagation in biological tissues: a beam-tracking method, IEEE Trans. Ultrason. Ferroelectrics Freq. Control 33 (4) (1986) 359–368.
[17] M. Kondo et al., An evaluation of an in vivo local sound speed estimation technique by the crossed beam method, Ultrasound Med. Biol. 16 (1) (1990) 65–72.
[18] I. Céspedes, J. Ophir, Y. Huang, On the feasibility of pulse-echo speed of sound estimation in small regions: simulation studies, Ultrasound Med. Biol. 18 (3) (1992) 283–291.
[19] M. Jaeger et al., Computed ultrasound tomography in echo mode for imaging speed of sound using pulse-echo sonography: proof of principle, Ultrasound Med. Biol. 41 (1) (2015) 235–250.
[20] M. O'Donnell et al., Internal displacement and strain imaging using ultrasonic speckle tracking, IEEE Trans. Ultrason. Ferroelectrics Freq. Control 41 (3) (1994) 314–325.
[21] B. Park et al., Predicting intramuscular fat in beef longissimus muscle from speed of sound, J. Anim. Sci. 72 (1994) 109–116.